Shock Sensitivity in Parabolized Navier-Stokes Solution of High Angle-of-Attack Supersonic Flow

D. D. Cline* and G. F. Carey†
University of Texas at Austin, Austin, Texas

Previous investigations with PNS/shock-fitting algorithms suggest that the lee-side shock profile is overly sensitive to the initial data when the angle of attack becomes large. The nature of this sensitivity is identified in the present work through an eigenvalue analysis of the coefficient matrices of the associated Euler system. These eigenvalues are evaluated along the evolving shock boundary and determine the relative amount of local numerical dissipation in the marching scheme. A significant disparity in the magnitude of the eigenvalues implies highly nonuniform damping of numerical errors along the shock boundary. Using eigenvalue estimates to deduce the PNS stepsize adaptively, and accounting for disparity in the eigenvalues, yields improved predictions of high angle-of-attack supersonic flow as demonstrated in the supporting numerical studies. Shock-profile anomalies encountered by previous investigators can therefore be attributed to an increase in the sensitivity of the PNS solution to the initial data as angle of attack is increased.

Introduction

THE PNS equations are derived from the full Navier-Stokes equations by eliminating the unsteady terms and neglecting the contribution of viscous derivatives in the streamwise direction. The resulting equation set is valid in both the inviscid and viscous regions of the flow with all the effects of second-order boundary-layer theory included. Thus, the PNS equations are particularly well-suited for calculating flowfields where there is strong interaction between the inviscid and viscous regions of the flow.[1-5] A relevant example of strong interaction is the supersonic flow past a slender body at high angle of attack. Here the effects of crossflow viscous separation are observed to extend over a significant portion of the lee-side region.

Results from previous investigations of PNS/shock-fitting algorithms suggest that the stability of the lee-side shock solution may deteriorate as the angle of attack is increased.[6,7] Attempts to stabilize the scheme usually rely on "artificial smoothing terms" appended to the algorithm in order to add additional dissipation. The effects of vehicle geometry, Mach number, and grid refinement all contribute to complicate the stability issue while reducing the robustness of the PNS/shock-fitting algorithm for high angle-of-attack flows.

To understand the lee-side sensitivity associated with high angle of attack calculations, we may consider the downstream propagation of errors in the initial data under conditions of varying angle of attack. As stated previously, the PNS equations are uniformly valid in both the viscous and inviscid regions of the flow. In the viscous region near the body, initial errors in the data are dissipated primarily through the diffusive effects of viscosity. However, for the inviscid region toward the shock, errors in the data are propagated downstream along characteristics and are dissipated only through the action of numerical viscosity which arises due to truncation error. These characteristics, and their variation with angle of attack, play an important role in determining the manner in which initial errors in the inviscid region are dissipated and are central to the present study.

In the present work, the effects of errors in the initial data prescribed for PNS/shock-fitting algorithms is investigated for "conical" bodies under conditions of high angle of attack. A conical "scaling" procedure is employed to examine the relationship between the shock Courant number, based on the local characteristic slope, and the evolution of the initial shock profile. It will be shown that the local dissipation of errors in the shock profile is controlled by the shock Courant number distribution along the shock boundary. This local shock Courant number can be established by means of an associated eigenvalue analysis. The sensitivity of the downstream solution to such parameters as angle of attack and cross-sectional geometry can then be assessed by comparison of the Courant number distributions.

In the first section, we state concisely the governing PNS equations, approximation assumptions, and data so that the basic methodology in question is clearly defined. Results of an eigenvalue analysis are then given for this formulation and used in the final section to explain the behavior of computed solutions. The present analysis offers improved solution capability for high angle-of-attack flows while providing a clear understanding of the shock-stability issue and associated anomalies in the lee-side shock profiles computed by previous investigators.

PNS Formulation

The parabolized Navier-Stokes (PNS) equations represent a mixed system of hyperbolic/parabolic equations for which a streamwise marching scheme is well-posed provided that certain conditions are met. Computational advantages of such a procedure over solution of the full Navier-Stokes equations include more rapid solution algorithms and less machine storage requirements. In the present formulation, the PNS equations are cast in generalized coordinates $\xi(x,y,z)$, $\eta(x,y,z)$, and $\zeta(x,y,z)$, where ξ denotes the streamwise or marching direction, with η and ζ being the normal and crossplane directions, respectively. The PNS equations may then be written in nondimensional form,[8]

$$\frac{\partial \bar{E}}{\partial \xi} + \frac{\partial \bar{F}}{\partial \eta} + \frac{\partial \bar{G}}{\partial \zeta} = 0 \tag{1}$$

Received April 4, 1988; revision received March 25, 1989.

*Professor, Department of Aerospace Engineering and Mechanical Engineering. Currently at Saudia National Laboratories, Albuquerque, NM.

†Professor, Department of Aerospace Engineering and Engineering Mechanics.

where the flux vectors $\bar{E}$, $\bar{F}$, and $\bar{G}$ are functions of the solution vector for three-dimensional flow

$$\bar{U}^t = \frac{1}{J}[\rho, \rho u, \rho v, \rho w, \rho e_t] \tag{2}$$

with density ρ, velocity components u, v, w, and total energy e_t. The flux vectors may be separated to inviscid and viscous parts as follows:

$$\bar{E} = \frac{1}{J}[\xi_x E + \xi_y F + \xi_z G] \tag{3a}$$

$$\bar{F} = \frac{1}{J}[\eta_x(E - E_v) + \eta_y(F - F_v) + \eta_z(G - G_v)] \tag{3b}$$

$$\bar{G} = \frac{1}{J}[\zeta_x(E - E_v) + \zeta_y(F - F_v) + \zeta_z(G - G_v)] \tag{3c}$$

In the above notation, J represents the Jacobian of the generalized transformation while ξ_x, η_y, etc. represent the generalized metrics. Elements of the respective inviscid and viscous flux vectors E, F, and G are given in Ref. 8.

The equation of state for a perfect gas which is compatible with the dimensionless equation set is assumed, while an equivalent form of Sutherland's law provides for temperature-dependent viscosity. All calculations presented herein assume laminar flow conditions.

Because of their parabolic/hyperbolic nature, the PNS equations enable three-dimensional flowfields to be obtained by marching an initial plane of data downstream. In subsonic regions, upstream effects are introduced through the streamwise pressure gradient in the streamwise momentum equation.[4] The streamwise pressure gradient must be modified in subsonic regions to eliminate upstream influences and maintain a stable marching scheme. A technique for modifying the streamwise pressure gradient developed by Vigneron et al.[1] is used in the present formulation.

At the body surface, the usual no-slip, no-injection conditions are required for the three components of velocity. An isothermal wall temperature is specified to satisfy a fourth boundary condition. Finally, a fifth condition requires the pressure gradient normal to the wall be set to zero. Along the planes of symmetry, simple reflective conditions are employed.

At the outer boundary of the flow domain, the bow shock surrounding the vehicle is fitted using a technique attributed to Thomas et al.[9] Variations of this shock-fitting algorithm have been previously used in a number of applications.[2,10,11] The formulation described herein was originally developed by Vigneron et al.[1] and later modified by Venkatapathy[12] for generalized coordinates. The procedure, which is sometimes referred to as the "pressure method," utilizes the pressure calculated behind the shock in conjunction with the Rankine-Hugoniot relations to determine the local shock slope. The shock standoff distance δ at the $(i+1)$ plane is calculated by explicit integration of the shock slope at plane (i) for the jth point along the shock boundary. Following the slope integration scheme, the next grid at plane $(i+1)$ is constructed. Currently, the grid may be constructed either from algebraic relations or by the solution of a coupled elliptic system. All results described in the present study were obtained with the algebraic grid scheme.

The initial shock shape is described by a two-segment elliptic cone which passes through the apex of the conical body. Flow properties behind the initial shock are calculated by an inverse application of the shock-fitting procedure, i.e., given the initial shock slope, the flow properties behind the shock may be determined from the Rankine-Hugoniot relationships and the freestream conditions. Distribution of initial values of the flow properties between the body and shock in the computational plane are given by simple trigonometric expressions.

The PNS equations are marched in ξ using the Euler-implicit formulation of the Beam-Warming algorithm.[13] The Euler-implicit formulation is unconditionally stable when applied to linearized systems of hyperbolic equations, i.e., the scheme is increasingly dissipative as the local Courant number increases. In the calculation of three-dimensional flows, the Courant number distribution controls the local dissipation in the inviscid region of the flow. As the angle of attack is increased, variation in the Courant number results in a crossplane variation in the amount of numerical damping produced in the algorithm. This effect is most evident when examining the Courant number distribution along the shock boundary which will be used to characterize the local sensitivity to initial conditions. In the following section, appropriate relationships are developed which define this distribution.

Eigenvalue Analysis

Analysis of the inviscid limit provides a conservative estimate for stepsize selection in PNS shock stability. In the inviscid limit of Eq. (1), the viscous flux vector contribution goes to zero. The resulting Euler system may be linearized with respect to the conserved variables given in Eq. (2) by expanding the appropriate derivatives using the following chain rules:

$$\frac{\partial \bar{E}}{\partial \xi} = \frac{\partial \bar{E}}{\partial \bar{U}}\frac{\partial \bar{U}}{\partial \xi} + \frac{\partial \bar{E}}{\partial \xi_x}\frac{\partial \xi_x}{\partial \xi} + \frac{\partial \bar{E}}{\partial \xi_y}\frac{\partial \xi_y}{\partial \xi} + \frac{\partial \bar{E}}{\partial \xi_z}\frac{\partial \xi_z}{\partial \xi} \tag{4a}$$

$$\frac{\partial \bar{F}}{\partial \eta} = \frac{\partial \bar{F}}{\partial \bar{U}}\frac{\partial \bar{U}}{\partial \eta} + \frac{\partial \bar{F}}{\partial \eta_x}\frac{\partial \eta_x}{\partial \eta} + \frac{\partial \bar{F}}{\partial \eta_y}\frac{\partial \eta_y}{\partial \eta} + \frac{\partial \bar{F}}{\partial \eta_z}\frac{\partial \eta_z}{\partial \eta} \tag{4b}$$

$$\frac{\partial \bar{G}}{\partial \zeta} = \frac{\partial \bar{G}}{\partial \bar{U}}\frac{\partial \bar{U}}{\partial \zeta} + \frac{\partial \bar{G}}{\partial \zeta_x}\frac{\partial \zeta_x}{\partial \zeta} + \frac{\partial \bar{G}}{\partial \zeta_y}\frac{\partial \zeta_y}{\partial \zeta} + \frac{\partial \bar{G}}{\partial \zeta_z}\frac{\partial \zeta_z}{\partial \zeta} \tag{4c}$$

Substituting the above relations into Eq. (1) yields the linearized form of Euler's equations,

$$\frac{\partial \bar{U}}{\partial \xi} + \left[\frac{\partial \bar{E}}{\partial \bar{U}}\right]^{-1}\left[\frac{\partial \bar{F}}{\partial \bar{U}}\right]\frac{\partial \bar{U}}{\partial \eta} + \left[\frac{\partial \bar{E}}{\partial \bar{U}}\right]^{-1}\left[\frac{\partial \bar{G}}{\partial \bar{U}}\right]\frac{\partial \bar{U}}{\partial \zeta} = \left[\frac{\partial \bar{E}}{\partial \bar{U}}\right]^{-1}\bar{H} \tag{5}$$

In the above equation, the vector $\bar{H}$ represents source terms originating from the derivatives taken with respect to the metrics. These source terms do not influence the characteristic structure of the equation set. Eigenvalues of the coefficient matrices $[\partial \bar{E}/\partial \bar{U}]^{-1}[\partial \bar{F}/\partial \bar{U}]$ and $[\partial \bar{E}/\partial \bar{U}]^{-1}[\partial \bar{G}/\partial \bar{U}]$ determine the relative slopes of the characteristic surfaces in the computational plane. For the (ξ,η) and the (ξ,ζ) planes, these eigenvalues will be denoted by λ_η and λ_ζ, respectively. Developing a closed-form solution for the eigenvalues presents a formidable task considering the relative complexity of the Jacobian elements. However, solution of the eigenvalue problem is feasible with the aid of a symbolic manipulator program. Symbolic algebraic equations representing the inviscid Jacobian elements were used as input to MACSYMA[14] in order to construct the characteristic equation which arises from the eigenvalue problem. Details of the linearization and symbolic analysis are provided in Ref. 15. For the (ξ,η) plane, the eigenvalues λ_η calculated using MACSYMA are

$$\lambda_\eta 1,2,3 = \frac{u\eta_x + v\eta_y + w\eta_z}{u\xi_x + v\xi_y + w\xi_z} \tag{6a}$$

$$\lambda_\eta 4,5 = \frac{(u\xi_x + v\xi_y + w\xi_z)(u\eta_x + v\eta_y + w\eta_z)}{(u\xi_x + v\xi_y + w\xi_z)^2 - c^2(\xi_x^2 + \xi_y^2 + \xi x_z^2)}$$

$$- \frac{c^2(\xi_x\eta_x + \xi_y\eta_y + \xi_z\eta_z) \pm c\sqrt{D\eta}}{(u\xi_x + v\xi_y + w\xi_z)^2 - c^2(\xi_x^2 + \xi_y^2 + \xi_z^2)} \tag{6b}$$

where the discriminate D_η consists of the following terms:

$$D_\eta = [(\eta_z\xi_x - \eta_x\xi_z)u - (\eta_y\xi_z - \eta_z\xi_y)v]^2 + [(\eta_x\xi_y - \eta_y\xi_x)u - (\eta_y\xi_z - \eta_z\xi_y)w]^2 + [(\eta_x\xi_y - \eta_y\xi_x)v - (\eta_z\xi_x - \eta_x\xi_z)w]^2 - c^2[(\eta_y\xi_z - \eta_z\xi_y)^2 + (\eta_z\xi_x - \eta_x\xi_z)^2 + (\eta_x\xi_y - \eta_y\xi_x)^2] \quad (6c)$$

and c is the local speed of sound. The analysis can also be performed for the eigenvalues λ_ζ in the (ξ,ζ) plane. These results are similar to those given above with the η metrics replaced by those in ζ.

The eigenvalues computed from Euler's equation are of significance to lee-side sensitivities in the coupled PNS/shock-fitting algorithm for two reasons. First, the maximum eigenvalue in Eq. (6b) provides a stability bound on the allowable streamwise marching step $\Delta\xi$ to ensure the explicit shock-fitting algorithm is stable. Second, the distribution of eigenvalues along the shock boundary controls the local numerical dissipation of solution error in the vicinity of the shock. The dissipation in the scheme determines the rate at which errors in the initial shock shape decay with the marching direction ξ. This dissipation may be directly related to the Courant numbers defined in the following section.

Crossplane Shock Courant Numbers

The eigenvalues presented in Eq. (6) form the basis for defining an effective Courant number for the spatially marching algorithm. The following definitions of Courant number in the computational plane follows the earlier work of Kutler et al.[11] for spatial marching of the Euler equations. Since the present analysis is carried out in computational coordinates, the results apply to all flow conditions and geometries compatible with the PNS assumptions.

For the (ξ,η) plane, the Courant number distribution for the spatial marching algorithm is given by

$$\mathrm{CFL}_\eta(\zeta) = \frac{|\lambda_\eta|_{\max,j}\Delta\xi}{\Delta\eta} \quad (7)$$

where $|\lambda_\eta|_{\max,j}$ is determined from the local maximum of the modulus of Eq. (6b) evaluated at each point j along the shock boundary. This is determined as follows:

$$|\lambda_\eta|_{\max,j} = \max(|\lambda_4|, |\lambda_5|)_j, \qquad j = 1,2,3 \ldots J_{\max} \quad (8)$$

The ζ dependency of CFL in Eq. (7) denotes the variation in the crossplane coordinate from the windward plane ($\zeta = 0$) to the leeward plane ($\zeta = 1$), along the shock boundary. Similarly for the (ξ,ζ) plane, the Courant number CFL_ζ as a function of ζ is determined from the maximum modulus of of λ_ζ as shown below:

$$\mathrm{CFL}_\zeta(\zeta) = \frac{|\lambda_\zeta|_{\max,j}\Delta\xi}{\Delta\zeta} \quad (9)$$

For stable explicit shock fitting, a sufficient condition then is

$$\mathrm{CFL}_{\max} = \max_\zeta (\mathrm{CFL}_\eta, \mathrm{CFL}_\zeta) < 1 \quad (10)$$

To provide further motivation for the analysis above, it is worthwhile to examine the dissipative properties of a simple model problem based on the two-dimensional wave equation. This represents an extension of the previous analysis given by Beam and Warming for the Euler implicit scheme applied to the simple wave equation.[13]

Dissipative Properties of the Euler Implicit Scheme

A model problem with properties similar to the Euler system in Eq. (5) is provided by the two-dimensional scalar wave equation

$$\frac{\partial u}{\partial \xi} + c_\eta \frac{\partial u}{\partial \eta} + c_\zeta \frac{\partial u}{\partial \zeta} = 0 \quad (11)$$

where the solution for u is obtained through "time-like" marching in the coordinate ξ. The two wave speeds, c_η and c_ξ, are assumed locally constant in accordance with the assumption of constant coefficient matrices in the linearized eigenvalue analysis. The wave speeds are analogous to the eigenvalues λ_η and λ_ζ in that they are proportional to the slopes of the characteristic curves in the (ξ,η) and (ξ,ζ) planes through a single step in ξ.

To study the stability of the two-dimensional wave equation, a standard von Neumann analysis is employed.[16] The von Neumann analysis considers the evolution of a solution error mode that can be represented by a two-variable complex Fourier series of the form

$$\epsilon(\xi,\eta,\zeta) = e^{\alpha\xi} e^{ik_m\zeta} e^{ik_n\eta} \quad (12)$$

Since the difference equation which results from application of the Euler implicit scheme to Eq. (11) is linear, the principle of superposition requires examination of only a single representative Fourier mode of the error as in Eq. (12). The error distribution may be substituted for u in the finite-difference analog to Eq. (11). Details of the stability analysis are standard and omitted here for brevity (for details see Ref. 17). From the von Neumann analysis, the amplification function G, which characterizes the dissipative properties of the implicit marching scheme, is given by

$$G = e^{\alpha\xi} = \frac{1 - v_\zeta v_\eta \sin\theta_\zeta \sin\theta_\eta}{(1 + iv_\zeta \sin\theta_\zeta)(1 + iv_\eta \sin\theta_\eta)} \quad (13)$$

where the angles θ_ζ and θ_η define angular equivalents of the wave numbers on the intervals $0 \le \theta_\zeta \le \pi$ and $0 \le \theta_\eta \le \pi$. That is, θ_ζ and θ_η are defined as

$$\theta_\zeta = km\Delta\zeta \quad (14a)$$

$$\theta_\eta = kn\Delta\eta \quad (14b)$$

where k_m and k_n are the wave numbers in Eq. (12). The Fourier components of lowest frequency correspond to $\theta_\zeta = 0$ and $\theta_\eta = 0$, while those of highest frequency are given by $\theta_\zeta = \pi$ and $\theta_\eta = \pi$.

Clearly for stability of the marching algorithm, it is required that the amplification factor for an initial disturbance satisfy

$$|G| \le 1 \quad (15)$$

This ensures that the amplitude of the error components are bounded for all component modes.

Solutions for $|G|$ were obtained from Eq. (13) for angular wave numbers on the intervals $0 \le \theta_\zeta \le \pi$ and $0 \le \theta_\eta \le \pi$. These solutions are presented graphically in Fig. 1 for two values of the CFL numbers, v_ζ and v_η. Regions for which $|G| = 1$ indicate wave numbers of neutral stability, while deviations of $|G|$ from unity indicate wave numbers where the Fourier component of the error is dissipated ($|G| < 1$) or grows unbounded ($|G| > 1$). Notice the dependency of $|G|$ on CFL which indicates the Euler implicit scheme is increasingly dissipative as CFL increases.

As can be seen in the results for $|G|$, the Euler implicit scheme applied to the two-dimensional wave equation is strongly dissipative for intermediate wave numbers provided that the CFL number is sufficiently large. It is therefore expected that in marching the PNS equations with this scheme, solution errors will be strongly dissipated in inviscid regions where the CFL number is relatively large. Inviscid regions for which the local CFL number is relatively small will encounter

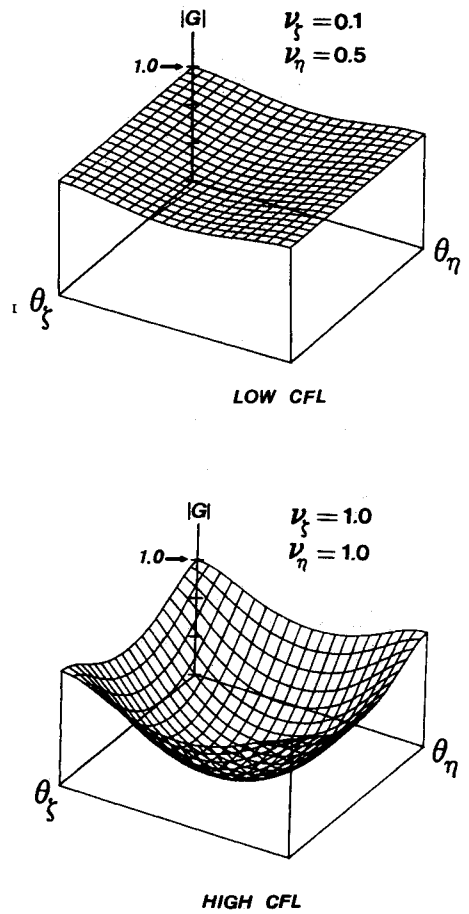

Fig. 1 Amplification factor of the solution algorithm for various CFL.

less dissipation with a corresponding increase in the solution's local sensitivity to errors in the initial data.

Shock Profile on Circular Cone at Angle of Attack

The present PNS solution for supersonic flow past bodies at high angle of attack requires the outer bow shock be "fitted" in accordance with the shock algorithm previously discussed. A systematic study of the interaction between the interior flow solution and the outer shock boundary was conducted to clarify the salient features of the bow-shock development. The focus of the present study is on the effect of variations in angle of attack and body geometry.

The experiments of Tracy[18] performed in the GALCIT hypersonic wind-tunnel facility were used to provide data for comparison with the PNS solutions. These experiments were performed on a sharp 10-deg cone in air at Mach 8, with a variation in angle of attack of up to 24 deg. The freestream Reynolds number was 4.59×10^5 based on a reference length of 11.71 cm, which corresponds to the axial length of the wind-tunnel model. The nominal wall temperature was 302.2K which was approximately 40% of the total freestream temperature. The Tracy experiments are of particular importance to the present study in that a pitot probe was traversed circumferentially around the cone to determine the bow-shock location.

The PNS starting solutions for the Tracy experiments were obtained by assuming an initial shock shape based on a two-segment elliptic cone. With the initial shock specified, the Rankine-Hugoniot relationships were used to determine the flow variables behind the shock and to construct the initial plane of data. This initial data plane was marched downstream a specified number of steps, after which the solution was conically scaled back to the original starting plane. This global sweeping was then repeated until the starting plane shock profile converged on successive sweeps. With this procedure, flow properties along conical rays are forced to be constant in accordance with inviscid conical flow theory. It is important to note that the solutions presented herein were generated without the use of artificial smoothing terms.

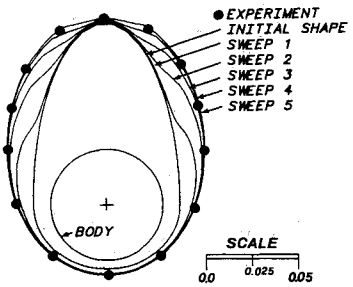

Fig. 2 Convergence of PNS bow-shock position and comparison with experiment for constant stepsize, $\alpha = 24$ deg.

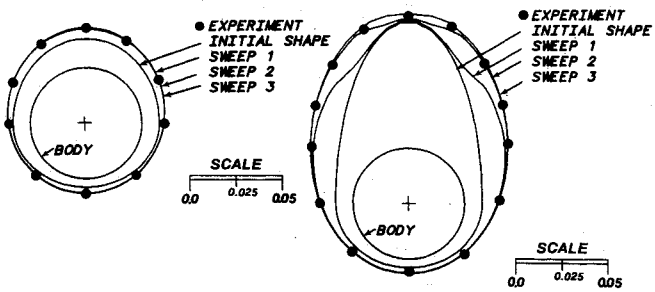

Fig. 3 Convergence of PNS bow-shock position and comparison with experiment for constant Courant number.

Figure 2 illustrates the development of the crossplane shock at an angle of attack of 24 deg. The scale provided measures distance as normalized by the cone reference length. The crossplane grid was constructed with 31 grid points normal to the body and 38 equally spaced circumferential lines. The solution shown was obtained using a constant marching step of $\Delta\xi = 4.15 \times 10^{-4}$ with each global sweep corresponding to 300 marching steps. Following each sweep, the solution plane was conically scaled to the starting plane at $\xi_0 = 0.17$. When marching at constant stepsize, the maximum shock Courant number decreases in the streamwise direction. For these cases, the maximum shock CFL number had a nominal value of 0.30. The shock profile shown following each global sweep illustrates the streamwise development of the shock. Notice that the shock profile does not develop uniformly, but rather develops first along the windward plane, then after further sweeps, becomes fully developed on the leeward plane. For constant stepsize marching, five global sweeps are required to achieve full shock development.

To study the effect of Courant number on the bow-shock development, the preceding calculations were repeated using the same grid parameters and initial data. The present solutions, however, were generated by marching the data plane with a constant maximum shock Courant number K. This requires the stepsize $\Delta\xi$ for the $(i + 1)$ solution plane be determined adaptively by maintaining $\mathrm{CFL}_{\max} = K$ at solution plane i. Here the constant K was taken to be 0.9. The crossplane shock profiles for solutions at 8 and 24 deg angle of attack are provided in Figs. 3a and 3b. Again 300 marching steps were used to define a single global sweep. Notice for the $\alpha = 8$-deg solution, only a single global sweep is necessary to achieve full development of the shock profile. The 24-deg solution required 3 global sweeps. Thus, it is evident that there is an angle-of-attack dependency in the number of sweeps needed to achieve full development of the shock profile. Comparison of the $\alpha = 24$-deg shock profiles with those presented in Fig. 2

indicates that the higher CFL solution achieved convergence of the bow shock with fewer global sweeps. As a further study of the stability of the shock-fitting algorithm, the previous case was recomputed with the CFL constant, $K = 1.01$. After 75 marching steps, the bow shock developed an unstable inflection on the windward plane which ultimately led to a failure in the shock-fitting algorithm.[15] In all cases studied with circular cones at angle of attack, the maximum shock Courant number was located along the windward plane. The normal plane Courant number CFL_η was dominant over the crossplane Courant number CFL. For circular cones, the stepsize criteria for a constant Courant number was dictated by the windward plane of value of CFL_η.

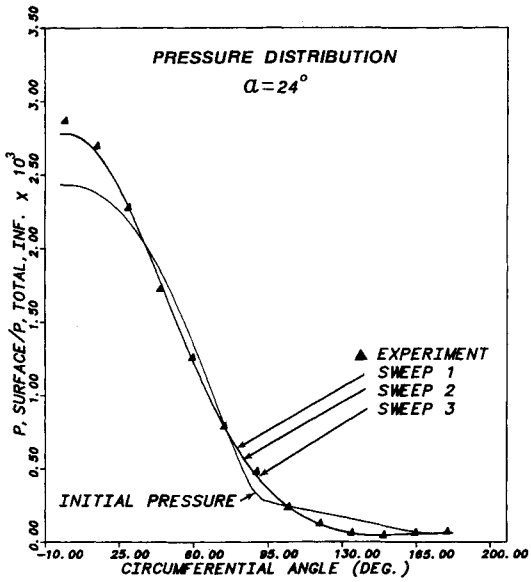

Fig. 4 Circumferential pressure distribution on Tracy cone surface at $\alpha = 24$ deg.

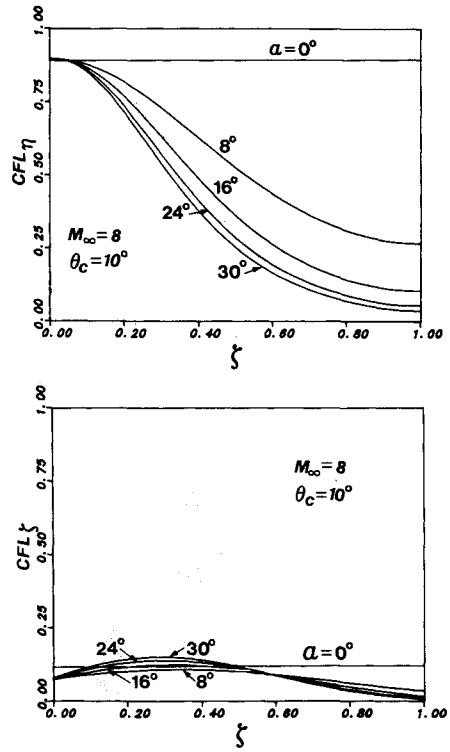

Fig. 5 Shock Courant number distribution as a function of angles of attack.

The circumferential distribution of wall pressure for the 24-deg case is compared in Fig. 4 with the experimental values measured by Tracy. The initial pressure distribution is assumed to be given by the shock pressure imposed to the wall. Note that the calculated wall pressure gives relatively good agreement with the experimental values after only a single global sweep. Thus, it is clear that the wall pressure does not adequately reflect the inaccuracies in the lee-side inviscid flow calculations which are present on subsequent sweeps.

Relationship between Local CFL and Angle of Attack

The previous results for the streamwise development of the shock profiles are best explained by examining the circumferential distribution of the two CFL numbers, CFL_η and CFL_ζ, along the shock boundary. The significance of the CFL distributions is clear when they are related to the dissipative properties of the two-dimensional wave equation studied in the previous section. That is, CFL_η and CFL_ζ are analogous to v_η and v_ζ in that they control the local amount of numerical dissipation in the normal and crossplane directions. It is this dissipation which damps initial errors in the shock profile and determines the manner in which the shock profile develops in the streamwise direction.

The Courant number distributions for the converged shock shapes generated for the Tracy cone are shown in Figs. 5a and 5b as a function of angle of attack. Also presented are distributions obtained at angles of attack of 0, 8, 16, and 30 deg. It is important to recall when examining these figures that $\zeta = 0$ and $\zeta = 1$ correspond to the windward plane region and leeward plane region, respectively. Notice that the computed values of CFL_η are greater than CFL_ζ over the entire shock boundary for all angles of attack. This indicates that the normal plane numerical dissipation is dominant over the dissipation in the crossplane. As the angle of attack is increased, the disparity between the windward plane and leeward plane values of CFL_η increases significantly. This is due to disparity in the shock eigenvalues computed from Eq. (6b). If Figs. 2 and 3 are re-examined, it is seen that the shock profile always develops from the windward plane to the leeward plane. In-

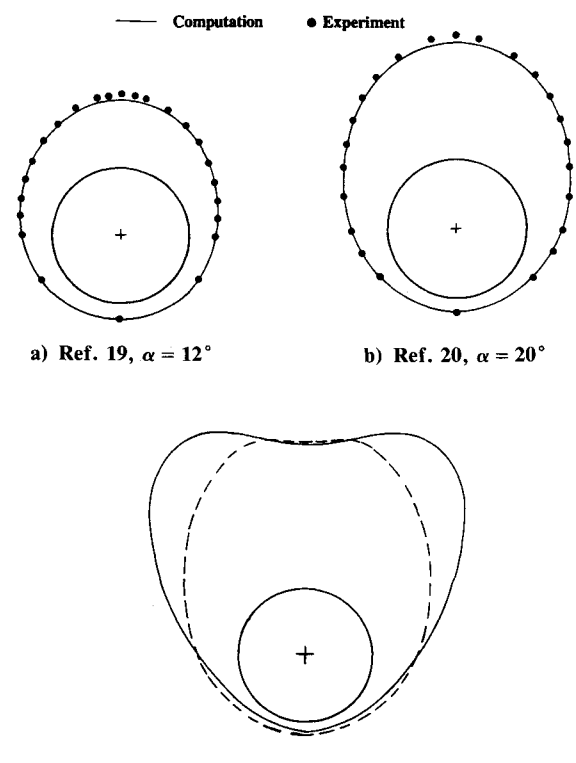

Fig. 6 Shock profiles for the Tracy cone reported by previous researchers.

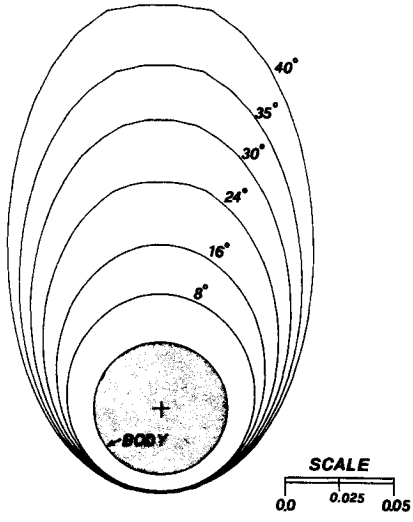

Fig. 7 Converged shock profiles for the Tracy cone at various angles of attack using the present techniques.

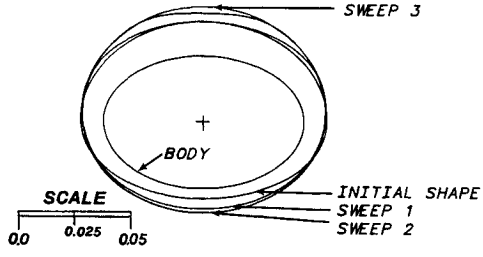

Fig. 8 Shock-profile development on an elliptic cone at 8-deg angle of attack with $M_\infty = 8$.

deed it is apparent that a great deal of computational effort is expended to converge the shock profile in the leeward plane region when the angle of attack is large. This result may be explained by considering the disparity in the shock CFL_η distribution. Along the windward side of the shock, the values of CFL_η are relatively large so that significant numerical damping of the solution occurs in this region. On the leeward side, CFL_η is relatively small so that very little damping of the solution occurs. Thus, initial errors in this region propagate over large distances, so that the downstream solution has an increasing sensitivity to perturbations in the initial data as the angle of attack is increased.

For the solution generated by taking a constant marching step, a lower value of CFL (CFL $\approx$ 0.3) requires more global sweeps to converge the shock due to an overall reduction in the amount of numerical dissipation. At the higher CFL, more numerical dissipation is introduced with a corresponding increase in the damping of initial errors.

Sensitivity of the lee-side shock profile to the initial data has been encountered by other researchers working with PNS codes which utilize the shock-fitting technique. For example, Figs. 6a–c illustrate computed shock profiles obtained from the literature[6,19,20] for the Tracy cone case at four different angles of attack. All three researchers utilize a shock-fitting technique to define the outer boundary of the flow domain. Notice that even for $\alpha = 12$ deg there is some disagreement with the experimental shock shape in the leeward plane region. Thus, the effect of the initial conditions on the accuracy of the downstream solutions is apparent even for relatively low angles of attack. Of particular interest are the shock profiles at $\alpha = 28$ and 45 deg computed by Lin and Rubin.[20] Their initial starting plane was constructed by enforcing the $\alpha = 28$- and 45-deg freestream boundary conditions on a numerically generated solution for a cone at 10-deg angle of attack. Note the

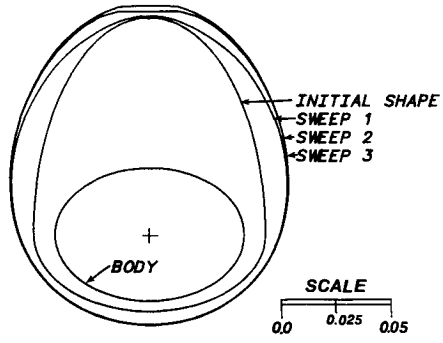

Fig. 9 Shock-profile development on an elliptic cone at 24-deg angle of attack with $M_\infty = 8$.

physically unrealistic concave inflection in the shock slope which occurs near the leeward plane of symmetry in each case. Further discussion of the $\alpha = 45$-deg solution provided in Ref. 7 indicated that the shock profile experienced strong oscillations on the leeward side as the solution was marched downstream.

At very high angles of attack, the lack of dissipation near the lee-side shock boundary makes it difficult to control the streamwise shock development without careful consideration of the Courant number distribution as well as the explicit CFL restriction imposed on the marching step. For comparative purposes, Fig. 7 provides predicted shock profiles for angles of attack ranging from 8–40 deg generated using the present technique. Stepsizes were calculated to ensure stability of the shock-fitting algorithm and each profile was globally marched until convergence was obtained on the leeward plane. No unstable lee-side inflections were encountered during the iteration process.

Shock Profile on Elliptic Cone at Angle of Attack

A further investigation into the relevant parameters which affect the streamwise shock development was conducted with the PNS code modified for cones of elliptic cross section. Solutions were obtained for an elliptic cone of unit eccentricity in the cross section with freestream conditions identical to the Tracy cone studies at Mach 8. The computational grid was constructed with 38 and 31 points circumferential and normal to the cone, respectively.

Figure 8 illustrates the streamwise shock development for the elliptic cone at 8-deg angle of attack. The shock convergence originates from the side plane with the point of convergence progressing more rapidly toward the windward plane than the leeward plane. Note that following the first global sweep (300 steps), the shock shape has changed very little from the initial shape on the leeward plane. The windward-plane shock converges after two global sweeps, whereas the leeward plane requires an additional 300 marching steps to achieve local convergence of the shock. Figure 9 shows the shock development at 24-deg angle of attack. In this case, the shock convergence originates along the windward side and proceeds to the leeward side in a manner very similar to the circular cone results.

The above results are reflected in the crossplane distributions for the Courant number CFL_η along the shock boundary. As seen in Fig. 10, the elliptic cross section has a marked effect on the distribution of CFL_η at relatively low angles of attack with the maximum Courant number (eigenvalue) occurring on the side plane, $\zeta = 0.5$. Thus, it is expected that the shock will converge first on the side plane due to the increased local dissipation there. As angle of attack is increased, the maximum Courant number shifts to the windward side as in the case for a circular cone. The crossplane distribution of numerical dissipation is therefore similar to that for a circular cone and the shock development proceeds from the windward plane to the leeward plane. The dominance of values for CFL_η over

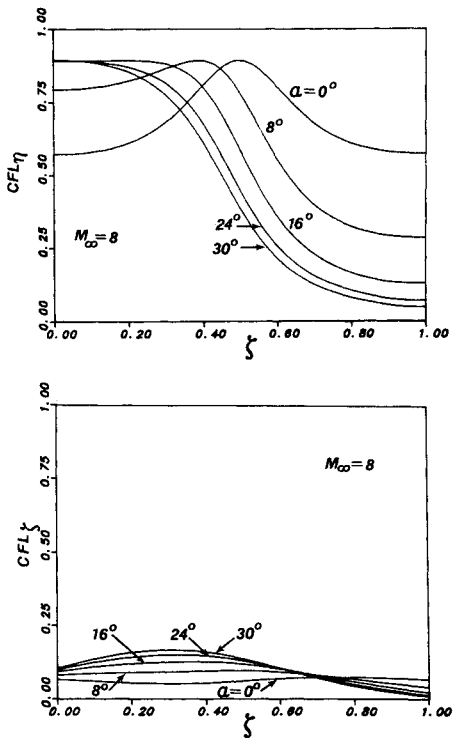

Fig. 10 Shock Courant number distribution as a function of angle of attack for the elliptic cone (compare Fig. 5).

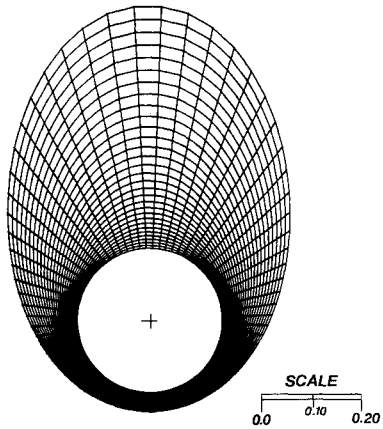

Fig. 11a Computational grid for crossplane section, α = 30 deg.

those for CFL$_\zeta$ reflect the greater dissipation in the normal plane.

High Angle of Attack Flowfield Solutions

The global sweep procedure enforces the condition that inviscid flow properties along conical rays are constant. The solution with the fully developed shock can therefore be used to approximate the initial plane of data for the PNS solution.

Solutions for the Tracy circular cone at an angle of attack of 30 deg were generated to illustrate the lee-side viscous-inviscid interaction which occurs under conditions of high angle of attack. The solution plane, taken as normal to the cone axis, was marched from $\xi = 0.17$ to the axial location $\xi = 0.81$. The maximum shock Courant number was held constant at 0.80. The grid size, node point distribution, and freestream conditions were identical to the previous case studies. Crossplane grid, velocity vectors, and isotherms for the flowfield as shown in Figs. 11a-c, respectively. Large gradients in the isotherms indicate regions where viscous effects dominate the flowfield.

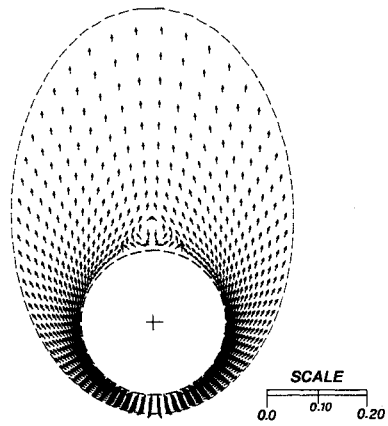

Fig. 11b Crossplane velocity vector field showing separation vortex, α = 30 deg.

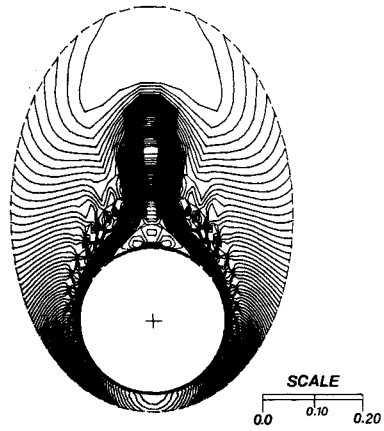

Fig. 11c Isotherms in the crossplane indicating regions of viscous interaction at high angle of attack.

Comparison of the velocity vectors with the isotherm plot reveals the embedded nature of the lee-side vortices. Solution of high angle of attack flows using the PNS equations with shock fitting requires that the lee-side region be carefully examined to ensure stability of the coupled algorithm and that errors in the initial inviscid flow data are dissipated.

Conclusions

Recent research efforts have been directed toward extending PNS schemes to more demanding flows such as those encountered for high angle of attack and toward improving the accuracy and stability of the solution algorithm. Problems with stepsize and the associated shock-stability problem can be circumvented by selecting conservative stepsizes to ensure shock stability at the expense of the overall computational efficiency of the PNS algorithm. However, the selection of a conservative stepsize is complicated by such factors as Mach number, angle of attack, body geometry, and grid resolution. The interaction of all these factors tends to reduce the robustness of the coupled PNS/explicit shock-fitting algorithm.

To improve this situation, an eigenvalue analysis of the Euler equations was performed in order to develop an appropriate Courant number restriction on the allowable marching step that is calculated adaptively as part of the solution procedure, and ensures the stability of the explicit shock-fitting procedure.

The streamwise development of the bow shock has been shown to be controlled by the local Courant number distribution along the shock boundary. When the angle of attack is small, the effect of cross-sectional geometry is apparent in the

Courant number distribution and thus the geometry influences the numerical dissipation in the inviscid region of the flow. As the angle of attack increases, disparate values of the shock eigenvalues lead to nonuniform numerical dissipation in the crossplane. Downstream solutions therefore exhibit a greater sensitivity to the initial data on the lee-side of the shock where the local dissipation in the numerical algorithm is small. As a result, poor lee-side shock predictions or inadvertent inflections in the lee-side shock profile may occur. This problem has been experienced by other researchers working with PNS codes which utilize a shock fitting procedure to define the computational boundary. It is believed that the present research provides the first plausible explanation for the increased sensitivity to the initial conditions at high angle of attack and an approach to circumvent this problem.

Because the normal plane Courant number dominates the stability of the scheme, variations in the circumferential grid spacing has little effect on the streamwise shock development. Disparate values in the distribution of shock eigenvalues were shown to occur, even at relatively low angles of attack ($\alpha/\theta_c < 1$). In general applications, however, combinations of Mach number, body geometry, or angle of attack may lead to a significant disparity in the shock eigenvalues with a corresponding increase in the solution's local sensitivity to the initial conditions.

Acknowledgments

This research has been supported in part by Boeing Company through a grant to the Computational Fluid Dynamics Laboratory at The University of Texas.

References

[1]Vigneron, Y. C., Rakich, J. V., and Tannehill, J. C., "Calculation of Supersonic Viscous Flow over Delta Wings with Sharp Subsonic Leading Edges," AIAA Paper 78-1137, July 1978.

[2]Rizk, Y. M., Chaussee, D. S., and McRae, D. S., "Computation of Hypersonic Viscous Flow Around Three-Dimensional Bodies at High Angles of Attack," AIAA Paper 82-1261, June 1981.

[3]Kaul, U. K. and Chaussee, D. S., "A Comparative Study of the Parabolized Navier-Stokes Code Using Various Grid-Generation Techniques," *Computers and Fluids,* Vol. 13, No. 4, 1985, pp. 421-441.

[4]Davis, R. T., Barnett, M., and Rakich, J. V., "The Calculation of Supersonic Viscous Flows Using the Parabolized Navier-Stokes Equations," *Computers and Fluids,* Vol. 14, No. 3, 1986, pp. 197-224.

[5]Schiff, L. B. and Steger, J. L., "Numerical Simulation of Steady Supersonic Viscous Flow," AIAA Paper 79-0130, Jan. 1979.

[6]Lin, A. and Rubin, S. G., "Three-Dimensional Supersonic Viscous Flow over a Cone at Incidence," AIAA Paper 81-0192, Jan. 1981.

[7]Lin, A. and Rubin S. G., "Three-Dimensional Supersonic Viscous Flow over a Cone at Incidence," *AIAA Journal,* Vol. 20, No. 11, 1981, pp. 1500-1507.

[8]Anderson, D. A., Tannehill, J. C., and Pletcher, R. H., *Computational Fluid Mechanics and Heat Transfer,* McGraw-Hill Book Company, New York, 1984, Ch. 8.

[9]Thomas, P. D., Vinokur, M., Bastianon, R. A., and Conti, R. J., "Numerical Solution for Three-Dimensional Inviscid Supersonic Flow," *AIAA Journal,* Vol. 10, No. 7, 1972, pp. 887-894.

[10]Chaussee, D. S., Patterson, J. L., Kutler, P., Pulliam, T., and Steger, J. L., "A Numerical Simulation of Hypersonic Viscous Flows over Arbitrary Geometries at High Angle of Attack," AIAA Paper 81-0050, Jan. 1981.

[11]Kutler, P., Warming, R. F., and Lomax, H., "Computation of Space Shuttle Flowfields Using Noncentered Finite-Difference Schemes," *AIAA Journal,* Vol. 11, No. 2, 1973, pp. 196-204.

[12]Venkatapathy, E., "A Generalized Solution Technique for the Parabolized Navier-Stokes Equations," Ph.D. Dissertation, Iowa State Univ., IA, 1982.

[13]Beam, R. M. and Warming, R. F., "An Implicit Factored Scheme for the Compressible Navier-Stokes Equations," *AIAA Journal,* Vol. 16, No. 4, 1978, pp. 393-402.

[14]*MACSYMA Reference Manual—Version 10*, Mathlab Group, Lab. for Computer Science, MIT, Cambridge, MA, Jan. 1983.

[15]Cline, D. D. and Carey G. F., "Symbolic Eigenvalue Analysis for Adaptive Stepsize Control in PNS Shock Stabilization" *Computers and Fluids*, Vol. 17, No. 4, 1989, pp. 527-535.

[16]Ferziger, J. H., *Numerical Methods for Engineering Application,* John Wiley & Sons, New York, 1981, Ch. 4.

[17]Cline, D. D., "The Effect of Disparate Shock Eigenvalues on the Numerical Solution of Supersonic Conical Flows," Ph.D. Dissertation, Univ. of Texas at Austin, Austin, TX, 1987.

[18]Tracy, R. R., "Hypersonic Flow over a Yawed Circular Cone," Ph.D. Dissertation, California Inst. of Technology, Pasadena, CA, 1963.

[19]Helliwell, W. S. and Lubard, S. C., "An Implicit Method for Three-Dimensional Viscous Flow with Application to Cones at Angle of Attack," *Computers and Fluids,* Vol. 3, No. 1, 1975, pp. 83-101.

[20]Lin, T. C. and Rubin, S. G., "A Numerical Model for Supersonic Viscous Flow over a Slender Reentry Vehicle," AIAA Paper 79-0205, Jan. 1979.